

1 Running title: An endocytic myosin-1 generates power

2

3 **Endocytic myosin-1 is a force-insensitive, power-generating motor**

4 Ross TA Pedersen<sup>1,3,4</sup>, Aaron Snoberger<sup>2,4</sup>, Serapion Pырpassopoulos<sup>2</sup>, Daniel Safer<sup>2</sup>, David

5 G Drubin<sup>1\*</sup>, E Michael Ostap<sup>2\*</sup>

6

7 <sup>1</sup>Department of Molecular and Cell Biology, University of California, Berkeley, Berkeley, CA

8 94720

9 <sup>2</sup>Pennsylvania Muscle Institute, Perelman School of Medicine, University of Pennsylvania,

10 Philadelphia, PA 19104

11 <sup>3</sup>Present address: Department of Embryology, Carnegie Institution for Science, Baltimore,

12 MD 21218

13 <sup>4</sup>Equal Contribution

14 \*Correspondence: [drubin@berkeley.edu](mailto:drubin@berkeley.edu), [ostap@mail.med.upenn.edu](mailto:ostap@mail.med.upenn.edu)

15 **Summary**

16

17 Pedersen, Snoberger et al. measure the force-sensitivity of the yeast endocytic the myosin-

18 1 called Myo5 and find that it is more likely to generate power than to serve as a force-

19 sensitive anchor in cells. Implications for Myo5's role in clathrin-mediated endocytosis are

20 discussed.

21 **Abstract**

22 Myosins are required for clathrin-mediated endocytosis, but their precise molecular roles  
23 in this process are not known. This is, in part, because the biophysical properties of the  
24 relevant motors have not been investigated. Myosins have diverse mechanochemical  
25 activities, ranging from powerful contractility against mechanical loads to force-sensitive  
26 anchoring. To better understand the essential molecular contribution of myosin to  
27 endocytosis, we studied the in vitro force-dependent kinetics of the *Saccharomyces*  
28 *cerevisiae* endocytic type I myosin called Myo5, a motor whose role in clathrin-mediated  
29 endocytosis has been meticulously studied in vivo. We report that Myo5 is a low-duty-ratio  
30 motor that is activated ~10-fold by phosphorylation, and that its working stroke and actin-  
31 detachment kinetics are relatively force-insensitive. Strikingly, the in vitro  
32 mechanochemistry of Myo5 is more like that of cardiac myosin than like that of slow  
33 anchoring myosin-1s found on endosomal membranes. We therefore propose that Myo5  
34 generates power to augment actin assembly-based forces during endocytosis in cells.

## 35 Introduction

36

37 During clathrin-mediated endocytosis (CME), the plasma membrane invaginates and  
38 undergoes scission to become a cytoplasmic vesicle. Coat proteins like clathrin can deform  
39 membranes under low tension (Dannhauser and Ungewickell, 2012; Busch et al., 2015; Cail  
40 et al., 2022), but when membrane bending is resisted by membrane tension (Hassinger et  
41 al., 2017), the actin cytoskeleton drives plasma membrane invagination (Boulant et al.,  
42 2011; Kaplan et al., 2022). In yeasts, including *Saccharomyces cerevisiae* and  
43 *Schizosaccharomyces pombe*, turgor pressure opposes plasma membrane invagination, so  
44 actin is required at every CME site (Aghamohammadzadeh and Ayscough, 2009; Basu et al.,  
45 2013).

46 The actin cytoskeleton can produce pushing and pulling force, both of which are  
47 required for CME in *S. cerevisiae* (Sun et al., 2006). When actin filament ends grow against a  
48 surface, they push the surface forward (Mogilner and Oster, 1996, 2003). During CME, actin  
49 filaments, bound by coat proteins, grow against the plasma membrane at the base the CME  
50 site, driving invagination (Picco et al., 2015; Kaksonen et al., 2005, 2003; Skruzny et al., 2012,  
51 Fig. 1). Modeling of the homologous CME machinery in mammalian cells has demonstrated  
52 that such actin networks generate sufficient power for CME (Akamatsu et al., 2020), but  
53 whether actin assembly alone can overcome turgor pressure in yeast cells is under debate  
54 (Nickaeen et al., 2019; Carlsson, 2018).

55 Additional power may be provided by myosins, which generate tension on actin  
56 filaments. The myosins critical for CME, Myo3 and Myo5 in budding yeast, and Myo1e in  
57 vertebrates, are type I myosins (Geli and Riezman, 1996; Cheng et al., 2012; Krendel et al.,

58 2007). Some type I myosins are well-suited to generate power – i.e., they carry out  
59 mechanical work per unit time by consuming ATP to execute a power stroke. Other type I  
60 myosins are ideally suited to serve as force-sensitive anchors – their ATPase cycle is easily  
61 arrested by resistance, locking them in a state that maintains tension without completing the  
62 ATPase cycle or powering movement (Greenberg and Ostap, 2013). The possible roles of  
63 type I myosins in CME depend on whether endocytic myosins are power generators or force-  
64 sensitive anchors.

65         If endocytic type I myosins are acutely force-sensitive, they might organize the actin  
66 filaments of the endocytic actin network, while if they are less force sensitive, they could  
67 power plasma membrane invagination (Evangelista et al., 2000, Fig. 1). Myosin-1 motors  
68 form a ring at the base of CME sites, where the invaginated membrane meets the plasma  
69 membrane (Mund et al., 2018, Fig. 1). Yeast type I myosins serve at least one organizational  
70 function as a membrane anchor for the actin assembly machinery, a function associated  
71 with the non-motor tail of the molecules (Lewellyn et al., 2015), but motor activity is  
72 required in addition to membrane anchorage (Pedersen and Drubin, 2019). If endocytic  
73 myosin-1s are force sensitive anchors, they may serve a further organizational role by  
74 holding growing filaments in an optimal orientation for force generation (Fig. 1, left). If the  
75 myosins are power-generating motors, they may pull actin filament ends away from the  
76 plasma membrane, deepening the plasma membrane invagination and creating space for  
77 monomer addition and filament elongation (Fig. 1, right), a model supported by the  
78 observation that the actin assembly rate at CME sites depends on type I myosin motors in a  
79 dose-dependent manner (Manenschijn et al., 2019).

80           To distinguish between these possibilities, we measured the force sensitivity of the  
81 endocytic myosin Myo5 (not to be confused with the vertebrate type V myosin). Myo5 is  
82 insensitive to resistive force compared to related myosins. We therefore propose that Myo5  
83 actively powers CME. Because actin and myosin collaborate in a variety of membrane  
84 remodeling processes, we expect that these results will be instructive beyond CME.

## 85 Results and Discussion

86

### 87 Heavy Chain Phosphorylation Activates Myo5 ATPase Activity

88 To determine how force sensitive Myo5 is, we first needed to measure its unloaded  
89 kinetics. We purified a Myo5 construct containing the motor and lever domains from *S.*  
90 *cerevisiae* (Fig. 2A). Because phosphorylation of Myo5 at the TEDS site is required for most  
91 CME events and is thought to regulate Myo5's motor activity (Grosshans et al., 2006; Sun et  
92 al., 2006; Bement and Mooseker, 1995), we purified a phosphorylated version and an  
93 unphosphorylated version of the protein separately (See Materials and methods). p21  
94 activated kinase was used to phosphorylate the myosin at the TEDS site (S357), as  
95 determined by control experiments with an S357A mutant (Fig. S1). The phosphorylation  
96 state of preparations was judged to be uniform when ATP-induced actoMyo5 dissociation  
97 transients were well fit by single exponential functions (see below). The yeast light chain  
98 for Myo5, calmodulin (Cmd1, Geli et al., 1998) was purified from *E. coli* and included in  
99 excess in all experiments (Fig. 2A).

100 We measured the steady-state actin-activated ATPase activities of phosphorylated  
101 and unphosphorylated Myo5 using the NADH-coupled assay (De La Cruz and Ostap, 2009)  
102 in the presence of 0 - 80  $\mu\text{M}$  phalloidin-stabilized actin. Unphosphorylated Myo5 ATPase  
103 activity was largely insensitive to actin: the ATPase rate for at 0  $\mu\text{M}$  actin was 0.14  $\text{s}^{-1}$ , while  
104 the maximum ATPase rate measured was 0.39  $\text{s}^{-1}$  at 40  $\mu\text{M}$  actin. (Fig. 2B). Phosphorylation  
105 activated Myo5 ATPase activity by about 10-fold (Fig. 2B). The actin concentration  
106 dependence of the phosphorylated Myo5 ATPase rate ( $k_{\text{obs}}$ ) was well fit by:

$$107 \quad k_{\text{obs}} = v_0 \frac{V_{\text{max}}[\text{Actin}]}{K_{\text{ATPase}} + [\text{Actin}]} \quad \text{(Equation 1)}$$

108 From the fit, the actin concentration at half-maximum of the ATPase rate ( $K_{\text{ATPase}}$ ) was  
109 determined to be  $5.1 \pm 0.88 \mu\text{M}$ , and the maximum ATPase rate ( $V_{\text{max}}$ ) was found to be  $3.3 \pm$   
110  $0.15 \text{ s}^{-1}$  (Fig, 2B; Table 1).

111

## 112 **ATP Binding and ADP Release are Non-Rate Limiting for Myo5 ATPase Activity**

113 Resistive force impacts the rate of myosin detachment from actin, and two biochemical  
114 transitions, ADP release and subsequent ATP binding, determine the detachment rate.

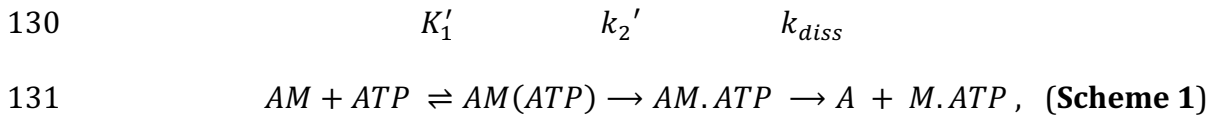
115 Therefore, we used stopped-flow kinetics to measure ADP release from (Fig. 2C,  $k_{+5}'$ ) and  
116 ATP binding to (Fig. 2C,  $K_1'$  and  $k_{+2}'$ ) actomyo5.

117 We found that yeast Myo5 does not quench the fluorescence of actin labeled at cys-374  
118 with pyrene iodoacetamide, which is the probe most used to measure actomyosin  
119 attachment and detachment (De La Cruz and Ostap, 2009). Thus, we measured actomyo5  
120 detachment by monitoring light scattering, which decreases as myosin unbinds actin.

121 To determine the rate constant for ATP binding, we mixed nucleotide-free actomyo5  
122 (100 nM) with varying concentrations of ATP and monitored  $90^\circ$  light scattering in the  
123 stopped-flow instrument. Light scattering time courses followed single exponential  
124 functions (Fig 2D). For phosphorylated Myo5, the observed rates determined from the fits  
125 increased linearly with ATP concentration (Fig. 2E). At concentrations of  $> 1 \text{ mM}$  ATP, the  
126 actomyosin complex dissociated within the response time of the instrument, precluding  
127 measurement. For unphosphorylated Myo5, the observed rates fit a rectangular hyperbola  
128 with increasing ATP concentration (Fig. 2E).



129 The mechanism was modeled as (De La Cruz and Ostap, 2009):

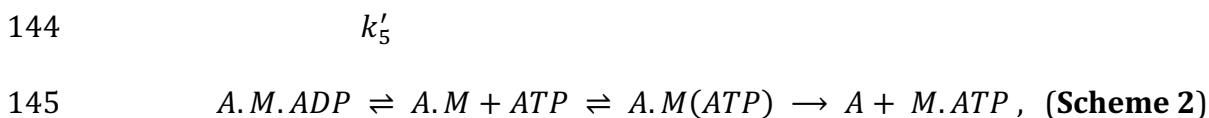


132 where  $K_1'$  is a rapid equilibrium binding step,  $k_2'$  is a rate-limiting isomerization to the  
133 AM.ATP state, and  $k_{diss}$  is the rapid actin dissociation step. The apparent second order rate  
134 constant for ATP binding to phosphorylated actoMyo5 was determined by a linear fit to the  
135 data ( $K_1'k_2' = 0.39 \pm 0.017 \mu\text{M}^{-1} \text{s}^{-1}$ ). The unphosphorylated actoMyo5 data were fit by:

$$136 \quad \quad \quad k_{obs} = \left[ \frac{K_1' [ATP]}{1 + K_1' [ATP]} \right] k_2', \quad (\text{Equation 2})$$

137 and the maximum rate of isomerization ( $k_2' = 290 \pm 24 \text{s}^{-1}$ ) and ATP affinity ( $K_1' = 0.006 \pm$   
138  $0.0016 \mu\text{M}^{-1}$ ) were determined. The apparent second-order rate constant for ATP binding  
139 ( $K_1'k_2'$ ) was determined from a linear fit of the observed rates below  $100 \mu\text{M}$  ATP to be  $1.1$   
140  $\pm 0.28 \mu\text{M}^{-1} \text{s}^{-1}$  (Table 1).

141 The rate constant for ADP dissociation ( $k_{+5}'$ ) was measured by preincubating  
142  $100 \mu\text{M}$  ADP with  $200 \text{ nM}$  actoMyo5 and then rapidly mixing with  $2.5 \text{ mM}$  ATP as shown in  
143 **scheme 2:**



146 When myosin active sites are saturated with ADP, the rate of ATP-induced dissociation of  
147 actomyosin is limited by ADP's slow dissociation. Light scattering transients were fitted by  
148 single exponential functions, yielding rates for ADP release for phosphorylated actoMyo5  
149 ( $k_{+5}' = 74 \pm 2.0 \text{s}^{-1}$ ) and for unphosphorylated actoMyo5 ( $k_{+5}' = 107 \pm 5.9 \text{s}^{-1}$ ) (Fig. 2F and  
150 Table 1). The signal-to-noise ratio of the fast light scattering transients is low, resulting in  
151 large uncertainties on these fits. However, these rates are substantially faster than the

152 steady-state ATPase values, but slower than the maximum rate of ATP-induced actomyosin  
153 dissociation. ADP release for actoMyo5 ADP is much faster than ADP release for vertebrate  
154 Myo1b and Myo1c (Greenberg et al., 2012; Lewis et al., 2006). It is more similar to the  
155 vertebrate endocytic myosin-1, Myo1e (El Mezgueldi et al., 2002). Because ADP release is  
156 rate limiting for detachment of Myo5 and Myo1e from actin, fast ADP release by these  
157 molecules mean that the unloaded actin-attachment lifetimes for endocytic type I myosins  
158 are < 15 ms. This property may make these motors particularly well-suited to function in  
159 dynamic actin networks like those at CME sites, where actin filaments elongate and  
160 “treadmill” into the cytoplasm (Kaksonen et al., 2003, 2005).

161

### 162 **Actin gliding is dependent on Myo5 phosphorylation state**

163 Our kinetic results suggest that both phosphorylated and unphosphorylated Myo5 have  
164 low duty ratios (i.e., the motor spends a small fraction of its ATPase cycle bound to actin).  
165 Since ADP release limits the rate of phosphorylated Myo5 detachment from actin at  
166 saturating ATP ( $k_{+5}' = 74 \pm 2.0 \text{ s}^{-1}$ ) and since we have measured the overall ATPase rate  
167 ( $V_{\max} = 3.3 \pm 0.15 \text{ s}^{-1}$ ), we can estimate the duty ratio:

$$168 \quad \text{Duty Ratio} = \frac{\left(\frac{1}{k_{+5}'}\right)}{\left(\frac{1}{V_{\max}}\right)}, \quad \text{(Equation 3)}$$

169 The calculated duty ratio of phosphorylated Myo5 is 0.045. Unphosphorylated Myo5 has a  
170 lower duty ratio (< 0.004).

171 To assess the effect of phosphorylation on Myo5 motility, we performed in vitro  
172 motility assays at 1 mM ATP. Motors were attached site-specifically to coverslips coated  
173 with anti-His<sub>6</sub> antibody. Coverslips were incubated with a range of concentrations of

174 phosphorylated and unphosphorylated Myo5, creating a titration series of surface  
175 densities. At low Myo5 surface densities (incubation with  $\leq 30$  nM phosphorylated Myo5,  
176  $\leq 150$  nM unphosphorylated Myo5), actin filaments failed to bind the coverslip (Fig. 2G and  
177 movies S1 and S2). At higher concentrations, phosphorylated Myo5 moved actin filaments  
178 at velocities ranging from  $720 \pm 40$  nm/s (100 nM phosphorylated Myo5) to  $880 \pm 90$  nm/s  
179 (40 nM) (Fig. 2G and movie S1). These gliding velocities are considerably higher than those  
180 reported by Sun et al., 2006, possibly reflecting differences in the phosphorylation state of  
181 the purified Myo5 protein (see below) or differences in other motility assay conditions,  
182 such as light chain availability. Higher ( $> 5$ -fold) surface densities of unphosphorylated  
183 Myo5 were required to achieve smooth motility, but this motility occurred at a  
184 substantially slower speed,  $\sim 120$  nm/s (Fig. 2G and movie S2). While it is possible that  
185 residual phosphorylated Myo5 in the unphosphorylated prep contributed to this motility,  
186 Sun et al., 2006 similarly reported that Myo5 harboring TEDS site mutations moved actin  
187 filaments much more slowly. The slower actin gliding speed for unphosphorylated myosin  
188 was unexpected given the similar rates of ADP release between phosphorylated and  
189 unphosphorylated Myo5 (Table 1). It is possible that the our kinetics experiments have not  
190 determined the rate limiting step for detachment, but it is more likely that motility of the  
191 unphosphorylated myosin is limited by the slow attachment rate of the motor (Stewart et  
192 al., 2021), as suggested by the slow actin-activated ATPase rate. The activation of Myo5  
193 motility by phosphorylation could explain why fast, cargo-induced endocytosis, which  
194 involves rapid and dynamic actin turnover, requires phosphorylated Myo5, while slower  
195 constitutive endocytosis does not (Grosshans et al., 2006).

196

197 **Myo5's working stroke comprises two substeps that are consistent with unloaded**  
198 **kinetic measurements**

199 The kinetics of actin attachment durations and mechanics of single myosin molecules were  
200 measured using an optical trapping instrument that can detect sub-nanometer  
201 displacements with millisecond temporal resolution (Woody et al., 2018; Snoberger et al.,  
202 2021). We used the three-bead optical trapping geometry in which a biotinylated actin  
203 filament is held between two laser-trapped polystyrene beads coated with neutravidin,  
204 creating a bead-actin-bead dumbbell (Fig. 3A). Dumbbells were lowered onto pedestal  
205 beads that were sparsely coated with phosphorylated Myo5-His<sub>9</sub> bound to a surface-  
206 adsorbed anti-His<sub>6</sub> tag antibody. The positions of trapped beads were detected via  
207 quadrant photodiode detectors, and single actomyosin binding events were detected by the  
208 decrease in covariance of the positions of the two dumbbell beads (Fig. 3B-D).

209 Traces acquired at 1, 10, and 1000  $\mu\text{M}$  ATP reveal displacements and drops in  
210 covariance during actomyosin binding events. Individual points from covariance traces  
211 were fit by double gaussian distributions, with the thresholds for event detection indicated  
212 as dotted gray lines in Fig. 3 B-D. Event durations decreased with increasing ATP  
213 concentrations (Fig. 3 B-D, blue lines).

214 The myosin-1 working stroke has been shown to occur in two discrete substeps,  
215 with the first substep occurring with actin-activated phosphate release, and the second  
216 occurring with ADP release (Jontes et al., 1995; Veigel et al., 1999, Fig. 3E). The substeps  
217 can be characterized in optical trapping assays by ensemble averaging single interactions  
218 (Veigel et al., 1999; Chen et al., 2012; Laakso et al., 2008), where the detected events are

219 aligned at their beginnings and forward-averaged in time (Fig 3F-H, left), or aligned at their  
220 ends and reverse-averaged in time (Fig 3F-H, right).

221 Ensemble averages of Myo5 interactions showed a two-step working stroke at the  
222 three ATP concentrations, but the step-size was most accurately resolved at 10  $\mu\text{M}$  ATP  
223 (see Materials and methods). In this condition, an initial substep of 4.8 nm was followed by  
224 a second substep of 0.2 nm (Fig. 3G). We determined the lifetimes of the substeps by fitting  
225 the ensemble averages with single exponential functions. At 1  $\mu\text{M}$  ATP (Fig. 3F, left trace),  
226 the measured rate ( $> 30 \text{ s}^{-1}$ ) of the time-forward average was limited by the covariance  
227 smoothing window, but at 10 and 1000  $\mu\text{M}$  ATP (Fig. 3 G-H, left traces), the rates were  $49 \pm$   
228  $1.6$  and  $50 \pm 0.2 \text{ s}^{-1}$ , respectively (Fig. 3K) which are similar to the measured ADP release  
229 rate ( $k_{+5}'$ ,  $74 \pm 2.0 \text{ s}^{-1}$ , Table 1) supporting the model that the transition from state-1 to  
230 state-2 accompanies ADP release.

231 The kinetics of time-reversed averages reveal the lifetime of State 2 (Fig. 3F-H, right  
232 traces). Fitting single exponential functions to these traces reveals rates of  $0.59 \pm 0.003$  and  
233  $7.34 \pm 0.1 \text{ s}^{-1}$  at 1 and 10  $\mu\text{M}$  ATP, respectively (Fig. 3K). At 1000  $\mu\text{M}$  ATP, the observed rate  
234 ( $> 187 \text{ s}^{-1}$ ) was limited by the size of the covariance smoothing window (5.25 ms; Fig. 3K).  
235 The observed rates at 1 and 10  $\mu\text{M}$  ATP are consistent with the second order rate constant  
236 for ATP binding of  $0.39 \pm 0.017 \mu\text{M}^{-1}\text{s}^{-1}$  measured by stopped-flow kinetics ( $K_1'k_{+2}'$ ,  
237 Table 1).

238 We determined the detachment rates of actomyosin events by plotting the  
239 cumulative frequency of individual attachment durations and fitting a single exponential  
240 function to the data by maximum likelihood estimation (Fig. 3I). Data from 1 and 10  $\mu\text{M}$   
241 ATP were well fit by single exponentials with rates of 0.88 and  $6.87 \text{ s}^{-1}$ , respectively (Fig. 3I,

242 Fig. 3K). These rates match well with the observed rate of ATP binding (Table 1), as well as  
243 the fits for the reverse ensemble averages, indicating that at sub-saturating ATP (1 and 10  
244  $\mu\text{M}$ ), detachment is limited by ATP binding (Figure 3J, blue squares & gray diamonds, Fig.  
245 3K). Data from 1000  $\mu\text{M}$  ATP were best described as the sum of 2 exponentials, with the  
246 major rate of  $67.8\text{ s}^{-1}$  comprising 92.1% of the total, and a minor rate of  $11.6\text{ s}^{-1}$  comprising  
247 7.9% of the total (Fig. 3I, Fig. 3K). The major rate is consistent with both the observed ADP  
248 release rate and the measured forward ensemble average rates, indicating that at  
249 saturating ATP, ADP release limits detachment of actomyosin interactions (Fig. 3J, blue  
250 square and black diamond, Fig. 3K).

251

## 252 **Myo5 is a relatively force-insensitive motor**

253 To elucidate the force sensitivity of Myo5, we measured how its actin detachment rate was  
254 affected by mechanical force opposing the power stroke using an isometric feedback  
255 system that maintained the actin filament near its initial position (Takagi et al., 2006). The  
256 initial force applied to Myo5 in this system depends in part on where along the actin  
257 filament Myo5 stochastically binds, so this approach allowed measurement of attachment  
258 durations at a range of resistive forces (Fig. 4A). Plotting attachment durations as a  
259 function of force revealed a general trend of longer attachment durations at higher  
260 resisting forces. At each interaction force, attachment durations are exponentially  
261 distributed and, as expected based on prior isometric feedback experiments, the data  
262 appear noisy when plotted this way (Fig. 4A). Converting these data to detachment rates by  
263 binning them by force at every ten points, averaging, and taking the inverse of the  
264 attachment duration more clearly reveals the trend (Fig. 4B).

265 The force dependence of the Myo5 detachment rate was fit by the Bell Equation:

$$266 \quad k(F) = k_0 \cdot e^{\frac{-F \cdot d}{k_B T}} \quad \text{(Equation 4)}$$

267 where  $k(F)$  is the detachment rate at force  $F$ ,  $k_0$  is the detachment rate in the absence of  
268 load,  $d$  is the distance parameter (the distance to the force-dependent transition state and a  
269 measure of force sensitivity),  $k_B$  is Boltzmann's constant, and  $T$  is the temperature. Best fit  
270 parameters for  $k_0$  and  $d$  were determined by maximum likelihood estimation of the  
271 unaveraged data from Fig. 4A, incorporating the instrument response time (15-30 ms,  
272 Woody et al., 2016). The estimated detachment rate in the absence of force is  $67.6 \text{ s}^{-1}$ , in  
273 close agreement with the measured detachment rate under low load conditions at  $1000 \mu\text{M}$   
274 (saturating) ATP ( $67.8 \text{ s}^{-1}$ , Fig. 3K). The best fit value for the distance parameter,  $d$ , was  
275  $1.14 \text{ nm}$ .

276 To put Myo5's force sensitivity in context, we re-plotted the function describing the  
277 force-dependent actin detachment rate of Myo5 alongside the same curves for vertebrate  
278 Myo1b, Myo1c, and  $\beta$ -cardiac myosin, which have previously been determined by the same  
279 experimental approach (Fig. 4C, Laakso et al., 2010; Greenberg et al., 2012; Woody et al.,  
280 2018). The mechanochemistry of Myo5 ( $d = 1.14 \text{ nm}$ ) is most like that of  $\beta$ -cardiac (muscle)  
281 myosin ( $d = 1.3 \text{ nm}$ ), suggesting that it is well-suited for generating power. The difference  
282 between Myo5 and acutely force-sensitive Myo1b, a tension-sensitive anchor myosin ( $d =$   
283  $15 \text{ nm}$ ), is dramatic. From 0 to 2 pN of resistance, Myo1b attachment lifetimes slow from  
284  $\sim 600 \text{ ms}$  to  $\sim 45 \text{ s}$ , resulting in negligible power generation (Fig. 4D). Over the same  
285 interval, Myo5 attachment lifetimes slow very modestly from  $\sim 15 \text{ ms}$  to  $\sim 25 \text{ ms}$ , allowing

286 it to generate considerable power (Fig. 4D). Thus, Myo5 is unlikely to act as a force-  
287 sensitive anchor in cells and is more likely to power movements against a resisting load.

288

### 289 **Proposed function of type I myosin in clathrin-mediated endocytosis**

290 Myo5 is one of the best-studied myosin-1 proteins in vivo. Quantitative live cell imaging  
291 and electron microscopy have revealed that it is recruited to CME sites simultaneously with  
292 initiation of actin assembly, where it concentrates at the base of the site as membrane  
293 invagination proceeds (Jonsdottir and Li, 2004; Idrissi et al., 2008). Although it has long  
294 been appreciated that the presence (Geli and Riezman, 1996; Goodson et al., 1996) and  
295 mechanochemical activity (Sun et al., 2006) of type-1 myosins are required for CME, the  
296 mechanistic contribution of motor activity to the dynamic actin network was unknown.  
297 When it was discovered that some type I myosins are acutely force sensitive (Laakso et al.,  
298 2008), it became apparent that these motors could have mechanochemical activities that  
299 range from force-dependent anchoring to power generation during CME. However,  
300 distinguishing among these possibilities has been difficult in cells. Mutant Myo5 molecules  
301 lacking the motor head or bearing mutations intended to lock the ATPase in low and high  
302 actin affinity states each block CME, results that do not reveal the mechanochemical role of  
303 Myo5 (Lewellyn et al., 2015; Idrissi et al., 2012). Perhaps the most informative finding in  
304 cells has been the observation that varying the number of type I myosins at CME sites  
305 results in differences in actin assembly rates (Manenschijn et al., 2019). However, because  
306 resistive load remodels growing branched actin networks in complex ways (Bieling et al.,  
307 2016), even this finding did not clearly differentiate between the possible roles for  
308 endocytic myosin-1s.



309           Here we have shown that Myo5's motor generates power rather than forming force-  
310 sensitive catch bonds. The overall ATPase rate of Myo5 is slow relative to other power-  
311 generating myosins, but its power stroke and detachment from actin are fast, and they slow  
312 only modestly under load (Fig. 4C). Myo5's relative force insensitivity means it generates  
313 steady power against resistance (Fig. 4D). Because Myo3 and Myo5 can each support CME  
314 in the absence of the other, we suspect that Myo3 is similarly force-insensitive. Given the  
315 structural and functional homology between Myo5 and vertebrate Myo1e, together with  
316 the close agreement of their unloaded kinetics (El Mezgueldi et al., 2002), we also predict  
317 the Myo1e generates biologically relevant power.

318           Our finding that Myo5's kinetics are relatively force insensitive lead us to interpret  
319 the previously described dose dependence of actin assembly on the number of myosin-1s  
320 at endocytic sites to mean that this motor moves actin filaments at CME sites to power  
321 plasma membrane invagination and create space for new monomers to assemble  
322 (Manenschijn et al., 2019, Fig. 1, right). On the order of 300 myosin molecules (Myo3 and  
323 Myo5 combined) are present at CME sites, mostly where the invaginating membrane meets  
324 the plasma membrane (Mund et al., 2018; Idrissi et al., 2008; Sun et al., 2019; Picco et al.,  
325 2015). A related myosin, Myo1c, also binds membranes and can generate and sustain sub-  
326 piconewton forces parallel to the plane of the membrane, and greater forces when moving  
327 actin filaments away from the membrane or when diffusion within the bilayer is impeded  
328 (Pyrpassopoulos et al., 2016). Myo5's diffusion is likely to be impeded by the many proteins  
329 at the base of CME sites, and it may move actin filaments at an angle to the membrane it is  
330 bound to. Actin subunits "treadmill" towards the cytoplasm in endocytic actin networks at  
331 ~50-100 nm/s (Kaksonen et al., 2005, 2003), so Myo5's motility rate of 700-900 nm/s (Fig.

332 2G), which we would expect resistance to slow only modestly, is fast enough to do work on  
333 the actin network as it assembles. We therefore expect that the myosins power membrane  
334 invagination and relieve load to accelerate actin assembly during CME.

335       Type I myosins are involved in a variety of membrane reshaping events in cells,  
336 where they often interact with growing branched actin networks (Sokac et al., 2006;  
337 Almeida et al., 2011; Joensuu et al., 2014; Krendel et al., 2007; Cheng et al., 2012), but the  
338 relative contributions of myosin motor activity and actin assembly have rarely been  
339 resolved. Here, we demonstrated that a type I myosin critical for CME, a process well-  
340 known to be driven by actin assembly, generates power. Implication of endocytic type I  
341 myosin as a force-insensitive motor suggests that actin assembly and myosin power  
342 generation can be coordinated to do coherent work in membrane remodeling processes.

## 343 **Materials and methods**

344

### 345 **Reagents, proteins, and buffers**

346 ATP concentrations were determined spectrophotometrically after each experiment by  
347 absorbance at 259 nm,  $\epsilon_{259} = 15,400 \text{ M}^{-1}\text{cm}^{-1}$ . For all ATP solutions, one molar equivalent of  
348  $\text{MgCl}_2$  was included to make MgATP. Rabbit skeletal muscle actin was prepared and gel  
349 filtered (Spudich and Watt, 1971). Actin concentrations were determined  
350 spectrophotometrically by absorbance at 290 nm,  $\epsilon_{290} = 26,600 \text{ M}^{-1}\text{cm}^{-1}$ . All actin was  
351 stabilized with one molar equivalent of phalloidin (Sigma). Steady-state, transient, and  
352 single molecule experiments were performed at 20°C in KMg25 buffer (60 mM MOPS pH 7,  
353 25 mM KCl, 1 mM EGTA, 1 mM  $\text{MgCl}_2$ , 1 mM DTT). Apyrase VII was obtained from Sigma.  
354 Purity and concentration of purified proteins were determined by comparing in-gel  
355 Coomassie blue staining to staining of known amounts of bovine serum albumin (Pierce).  
356

### 357 **Expression and Purification of Cmd1**

358 The *S. cerevisiae* calmodulin gene *CMD1* was cloned from genomic DNA into a bacterial  
359 expression plasmid with a sequence encoding His<sub>6</sub>-TEV situated at the 5' end to generate  
360 pDD2743. pDD2743 was transformed into Rosetta *E. coli*, optimized for expression  
361 (Novagen). A saturated overnight culture in LB (10 g/L Bacto tryptone, 5 g/L Bacto yeast  
362 extract, 10 g/L NaCl) was used to inoculate a 1 L culture in LB to  $\text{OD}_{600} = 0.1$ . Cells were  
363 grown to  $\text{OD}_{600} = 0.6-1$ , induced with 0.5 mM IPTG for 5 hours at 37°C, pelleted at 4,225 x g  
364 for 20 minutes at 4°C in a Sorvall SLA-3000 (fixed angle) rotor, washed with cold 20 mM  
365 HEPES pH 7.5, and repelleted at 2,250 x g for 10 minutes at 4°C in a Jouan CR3i (swinging

366 bucket) centrifuge. Cell pellets were flash frozen in 45 mL lysis buffer (20 mM HEPES pH  
367 7.5, 1 M KCl, 20 mM Imidazole). Upon thawing, cells were lysed by sonication, 2 mg DNase I  
368 (Roche) and triton X-100 to 1% were added, and the resulting lysate was incubated on ice  
369 for 30 minutes, then spun at 92,000 x g for 25 minutes in a Beckman Type 70 Ti rotor. The  
370 supernatant was loaded onto a 1 mL HisTrap HP column (GE healthcare) preequilibrated  
371 with binding buffer (20 mM HEPES pH 7.5, 500 mM KCl, 20 mM imidazole). The column  
372 was washed with 20 mL binding buffer, and Cmd1 was eluted using a 30 mL linear gradient  
373 from 0-100% elution buffer (20 mM HEPES pH 7.5, 500 mM KCl, 500 mM imidazole).  
374 Fractions containing Cmd1 were pooled, Cmd1 was cleaved from His<sub>6</sub> with TEV protease  
375 and dialyzed overnight at 4°C into low salt buffer (10 mM Tris pH 7, 25 mM NaCl, 2 mM  
376 MgCl<sub>2</sub>, 5 mM DTT). Following dialysis, purified, cleaved Cmd1 was bound to a MonoQ  
377 column and eluted using a 10 mL linear gradient from 0-70% high salt buffer (10 mM Tris  
378 pH 7, 1 M NaCl, 2 mM MgCl<sub>2</sub>, 5 mM DTT). Fractions containing Cmd1 were pooled, dialyzed  
379 into KMg50 buffer (60 mM MOPS pH 7, 50 mM KCl, 1 mM MgCl<sub>2</sub>, 1 mM EGTA, 1 mM DTT,  
380 5% glycerol), and stored at -80°C.

381

## 382 **Expression and Purification of Myo5**

383 Myo5 was coexpressed with the myosin chaperone She4 in *S. cerevisiae*. The *MYO5* open  
384 reading frame (ORF) from *S. cerevisiae* was cloned from genomic DNA and truncated at  
385 Gly<sup>763</sup>, generating a construct containing the motor domain and both Cmd1-binding IQ  
386 motifs of the lever arm. The *SHE4* ORF was cloned in its entirety from *S. cerevisiae* genomic  
387 DNA. Both ORFs were ligated into a 2 $\mu$  expression plasmid with a partially defective *LEU2*  
388 gene (*leu2d*) to ensure high copy number, creating plasmid pDD2744 (parent vector

389 described in Roy et al., 2011). The *MYO5* ORF was situated with a sequence encoding  
390 AviTag-TEV-His<sub>9</sub> at the 3' end. Expression of the *MYO5* and *SHE4* ORFs was driven by a  
391 bidirectional Gal 1/10 promoter.

392 pDD2744 was transformed into D1074 yeast (Roy et al., 2011). Saturated overnight  
393 cultures in synthetic minimal medium (1.5 g/L Difacto yeast nitrogen base, 5 g/L  
394 ammonium sulfate, supplemented with 2% glucose 20 µg/mL adenine, L-histadine, L-  
395 methionine, and 30 µg/mL L-lysine) were used to inoculate 1.5 L cultures in the same  
396 media with raffinose substituted for glucose to OD<sub>600</sub> = 0.1. After 18 hours of growth at  
397 30°C, cultures were induced with 2% galactose, Bacto yeast extract was added to 10 g/L,  
398 and Bacto peptone to 20 g/L. After 8 hours of expression, the cells were harvested at 4,225  
399 x g for 20 minutes at 4°C in a Sorvall SLA-3000 rotor, washed with 25 mL cold Milli-Q  
400 water, repelleted at 2,250 x g for 10 minutes at 4°C in a Jouan CR3i centrifuge, resuspended  
401 in 0.2 volumes of cold Milli-Q water, and drop frozen into liquid nitrogen. Lysis was  
402 achieved through cryomilling (10 cycles of 3 minutes grinding with one minute cooldown)  
403 in the large vials of a 6870 freezer/mill (SPEX Sample Prep).

404 Cell powders were thawed in binding buffer (10 mM Tris pH 7, 500 mM NaCl, 4 mM  
405 MgCl<sub>2</sub>, 2 mM ATP, 20 mM imidazole, 5 mM DTT) supplemented with 1 mM PMSF, 1 x  
406 cOmplete protease inhibitor cocktail without EDTA (Roche), and 1 µM Cmd1. For  
407 purification of phosphorylated Myo5, 1 µg Pak1 (Sigma, Brzeska et al., 1997, Fig. S1) was  
408 included in the lysis buffer and 10 mM β-glycerophosphate, 5 mM sodium pyrophosphate,  
409 and 50 mM sodium fluoride were included in all purification buffers. For purification of  
410 unphosphorylated Myo5, 4000 units lambda phosphatase (NEB) and 1 mM MnCl<sub>2</sub> were  
411 included in the lysis buffer. The lysate was then spun at 345,000 x g for 10 minutes at 4°C

412 in a Beckman TLA100.3 rotor, filtered through a 0.22  $\mu\text{m}$  filter, and loaded onto a 1 mL  
413 HisTrap HP column. The column was washed with wash buffer (Binding buffer with only  
414 200 mM NaCl), and Myo5 was eluted using a 20 mL linear gradient from 0-100% elution  
415 buffer (wash buffer with 1 M imidazole).

416 Fractions containing Myo5 were pooled and supplemented with Cmd1 to 1  $\mu\text{M}$ . For  
417 unphosphorylated Myo5 purification, a further 20,000 units lambda phosphatase were  
418 added along with  $\text{MnCl}_2$  to 1 mM and the fractions were incubated at 30°C for 30 minutes.  
419 Purified protein was dialyzed through a 3.5 KDa MWCO membrane into 1 L storage buffer  
420 (KMg50 with 50% glycerol) overnight at 4°C and again into 500 mL of the same buffer for 2  
421 hours at 4°C, then stored at -20°C.

422

### 423 **Kinetic measurements**

424 Steady-state actin-activated ATPase activity was measured using the NADH enzyme-linked  
425 assay in an Applied Photophysics (Surrey, UK) SX.18 MV stopped-flow apparatus (De La  
426 Cruz and Ostap, 2009). One reaction syringe contained the ATP mix (200  $\mu\text{M}$  NADH, 20  
427 U/mL lactic dehydrogenase, 100 U/mL pyruvate kinase, 500  $\mu\text{M}$  phospho(enol)pyruvate, 2  
428 mM  $\text{MgCl}_2$ , 2 mM ATP in KMg25) and the other syringe contained the mixture of actin (0-80  
429  $\mu\text{M}$ ) and myosin (100 nM) in KMg25. Concentrations above are post-mixing. After mixing,  
430 the concentration of NADH loss due to ATP hydrolysis was monitored by absorbance at 340  
431 nm ( $\epsilon_{340} = 6,220 \text{ M}^{-1}\text{cm}^{-1}$ ), and the linear regions of the curve were fitted to a straight line  
432 to determine ATPase activity.

433 ATP-induced dissociation of actoMyo5 was measured and analyzed as described (De  
434 La Cruz and Ostap, 2009). Briefly, one reaction syringe contained ATP (0 – 2.7 mM) in

435 KMg25 and the other syringe contained 100nM Myo5 and 100 nM phalloidin-stabilized  
436 actin. Reactants were rapidly mixed by the instrument, and light scattering at 90° was  
437 acquired using a 450 nm excitation light and a 400 nm emission filter. Experimental  
438 transients were fit by single exponentials using the software provided with the stopped-  
439 flow apparatus. 1-7 traces were averaged together to generate each data point. 0.04  
440 units/mL apyrase was added to solutions of actoMyo5 before mixing to remove  
441 contaminating ADP and ATP. Unphosphorylated actoMyo5 required prolonged treatment  
442 with apyrase to achieve sufficient signal, presumably because a larger fraction of the  
443 population was bound to ATP left over from purification and because the actin-activated  
444 ATPase rate of unphosphorylated Myo5 is slow. ADP release transients were acquired and  
445 analyzed as above by preincubating 100 μM ADP with 200 nM actoMyo5 and then rapidly  
446 mixing with 2.5 mM ATP. Concentrations reported are post-mixing.

447

#### 448 **Motility assays**

449 Motility assays were carried out essentially as in (Lin et al., 2005). Double-sided Scotch  
450 tape and vacuum grease were used to create flow chambers from a clean glass coverslip  
451 (22 mm x 40 mm, #1.5, Fisher) and a glass coverslip coated with 20 μL nitrocellulose  
452 (Ernest F. Fullam, Inc., catalog number 11180). A mouse monoclonal antibody against His<sub>6</sub>  
453 (Sigma), made 0.2 mg/mL in motility buffer (10 mM MOPS pH 7, 25 mM KCl, 1 mM EGTA, 1  
454 mM MgCl<sub>2</sub>, 1 mM DTT), was first added to the flow chamber, and incubated there for 5  
455 minutes to coat the nitrocellulose-coated coverslip with the antibody. The flow chamber  
456 was then blocked for 2 minutes with 2 mg/mL casein. Blocking coverslips with bovine  
457 serum albumin (BSA) led to inferior gliding. Phosphorylated or unphosphorylated Myo5 in

458 motility buffer with 2 mg/mL casein, diluted to a range of concentrations as indicated in  
459 Fig. 2G, was added to the flow chamber and incubated for 2 minutes, then the chamber was  
460 washed once with motility buffer containing 1 mM ATP and 5  $\mu$ M Cmd1 and three more  
461 times with the same buffer without ATP. Motility was initiated by loading the chambers  
462 with 5 nM rhodamine phalloidin-labeled actin filaments in motility buffer with 1  $\mu$ M ATP, 5  
463  $\mu$ M Cmd1, 2 mg/mL casein, 0.4 mg/mL glucose oxidase, 0.08 mg/mL catalase, 5 mg/mL  
464 glucose. Movies of actin motility in the flow chambers were recorded at room temperature  
465 ( $\sim 20^{\circ}\text{C}$ ) on a Leica DMI3000 B microscope outfitted with a 100x, 1.4 NA plan apo objective  
466 and a Retiga R6 CCD camera (Teledyne), controlled by Metamorph software. The rate of  
467 actin filament gliding was determined using the manual tracking plugin in Fiji.

468

### 469 **Optical trapping**

470 Flow chambers for optical trapping were constructed with double-sided tape and vacuum  
471 grease as previously described (Snoberger et al., 2021; Greenberg et al., 2017). Briefly, the  
472 coverslip was coated with a 0.1% mixture of nitrocellulose and 2.47  $\mu$ m diameter silica  
473 beads. Coverslips were dried at least 30 minutes and were used within 24 hours of  
474 preparation. To define the walls of the flow cell, 2 strips of double-sided tape were placed  
475  $\sim 5$  mm apart, a 1 mm thick glass slide was placed on top, and carefully sealed with vacuum  
476 grease after addition of final buffer.

477 Trapping buffer (KMg25 with 1 mM DTT freshly added) was used for all trapping  
478 assays. A 100x stock of glucose oxidase + catalase (GOC) was freshly prepared by  
479 centrifuging catalase (Sigma,  $> 30000 \text{ U}\cdot\text{mL}^{-1}$ ) at 15,000 x g for 1 minute, and adding 2  $\mu$ l of  
480 catalase supernatant to 20  $\mu$ L of 19.1 U/ $\mu$ L glucose oxidase (Sigma).



481           0.01 mg/mL anti-His<sub>6</sub> antibody (Sigma) was flowed in the chamber and incubated  
482 between 30 seconds and 3 minutes, then immediately blocked with two, 3-minute  
483 incubations of 1 - 2 mg/mL BSA. Stocks of phosphorylated His<sub>9</sub>-tagged Myo5 were diluted  
484 to 1 nM in trapping buffer with 300 mM added KCl and incubated in the flow cell for 2  
485 minutes. The number of myosins bound to the surface was limited by the surface  
486 concentration of anti-His<sub>6</sub> antibody, and the incubation time of anti-His<sub>6</sub> antibody was  
487 adjusted daily between 30 seconds and 3 minutes such that 1 of 3 - 5 pedestals tested  
488 showed clear myosin interactions with the actin dumbbell.

489           Following incubation with Myo5, a second blocking step with two, 3-minute  
490 incubations of 1 - 2 mg/mL BSA was performed. Final buffer added to the flow cell  
491 contained trapping buffer with indicated amount of ATP, 1  $\mu$ L of GOC added immediately  
492 prior to addition to chamber, and 0.1 - 0.25 nM rabbit skeletal muscle actin polymerized  
493 with 15% biotinylated actin (Cytoskeleton) stabilized by rhodamine-phalloidin (Sigma) at a  
494 1.1-1.2 molar ratio with G-actin concentration. Neutraavidin-coated beads were prepared by  
495 incubating 0.4 ng of 0.8  $\mu$ m diameter polystyrene beads (Polysciences) and coated with 5  
496 mg/mL neutraavidin (Thermo Fisher). 3  $\mu$ L of neutraavidin-coated beads were added to one  
497 side of the chamber prior to sealing. All trapping data were acquired within 90 minutes of  
498 addition of the final buffer to the chamber.

499           Optical trapping experiments were performed at room temperature ( $20 \pm 1$  °C)  
500 using a dual beam 1064 nm trapping laser as described in (Woody et al., 2018, 2017). A  
501 single laser beam was split into 2 beams using polarizing beam splitters and steered into a  
502 60x water immersion objective (Nikon). Laser light was projected through an oil  
503 immersion condenser and into quadrant photodiodes (JQ-50P, Electro Optical Components,

504 Inc.), each of which were conjugate to the back focal plane of the objective. Direct force  
505 detection from the quadrant photodiodes was achieved using a custom-built high-voltage  
506 reverse bias and an amplifier. Data acquisition, beam position control output, and isometric  
507 feedback calculations were controlled with custom-built virtual instruments (Labview,  
508 Matlab).

509 Individual 0.8  $\mu\text{m}$  diameter neutravidin-coated bead were caught in the two traps  
510 and held approximately 5  $\mu\text{m}$  apart. Trap stiffnesses were adjusted to 0.05 – 0.1 pN/nm for  
511 each trap. A biotinylated actin filament visualized by rhodamine phalloidin was bound to  
512 the two trapped beads, creating a bead-actin-bead dumbbell. The dumbbell was  
513 pretensioned (3-5 pN) by steering one beam using a piezo controlled mirror conjugate to  
514 the back focal plane of the objective, and the surface of pedestal beads were probed for  
515 myosins. Putative myosin interactions were detected via drops in variance of the two  
516 beads, and the 3-dimensional position of the dumbbell relative to the myosin was refined  
517 further by maximizing the rate and size of the observed power stroke deflections. Every 30-  
518 60 s, the dumbbell was moved axially along the actin filament in  $\sim 6$  nm steps between  
519 trace acquisition to ensure even accessibility of actin-attachment target zones. Stage drift  
520 was corrected via a feedback system using a nano-positioning stage and imaging the  
521 position of the pedestal bead with nm precision (Woody et al., 2017). In experiments using  
522 1  $\mu\text{M}$  ATP, due to the longer actomyosin interactions, stage drift was still observed even  
523 with the stage feedback engaged, leading to a presumed underestimation of the  
524 displacement size. All data were acquired at a sampling rate of 250 kHz.

525 Isometric optical clamping experiments were performed as described in (Woody et  
526 al., 2018; Takagi et al., 2006) using a digital feedback loop and a 1-D electro-optical

527 deflector (EOD, LTA4-Crystal, Conoptics) to steer the beam position using input from a high  
528 voltage source (Conoptics, Model 420 Amplifier). Briefly, the position of one bead (the  
529 “transducer” bead) was maintained at a constant position by adjusting the position of the  
530 other bead (referred to as the “motor” bead) during actomyosin interactions. The response  
531 time of the feedback loop during actomyosin interactions was ~15-30 ms.

532

### 533 **Optical trap data analysis**

534 Actomyosin interactions for non-isometric optical clamping experiments were detected  
535 using the single-molecule computational tool SPASM (Software for Precise Analysis of  
536 Single Molecules, Blackwell et al., 2021), which uses a calculation of the dumbbell bead  
537 covariances and a change-point algorithm. Data collected at 1000  $\mu\text{M}$  ATP were analyzed at  
538 250 kHz, while data collected at 1 and 10  $\mu\text{M}$  ATP were downsampled to 2 kHz by  
539 averaging every 125 points to enhance analysis speed. Events were detected by calculating  
540 the covariance of the 2 beads using a smoothing window of 33.3, 15, and 5.25 ms and an  
541 averaging window 60, 36, and 12 ms at 1, 10, and 1000  $\mu\text{M}$  ATP, respectively. The  
542 instrument deadtime was calculated to be 2 times the covariance averaging window. For  
543 each 15 s trace, the detected covariance was plotted and fit to double gaussian  
544 distributions, with the smaller mean gaussian corresponding to the actomyosin “bound”  
545 portion and the larger mean gaussian corresponding to the “unbound” portion of events. A  
546 putative event was defined as an event where the covariance starts above the unbound  
547 peak mean, drops below the bound peak mean, and remains below the unbound peak mean  
548 for at least the length of the instrument deadtime prior to returning back above unbound  
549 peak mean. Event starts and ends were further refined using a changepoint algorithm as

550 described (Blackwell et al., 2021). Attachment durations and ensemble averages of single  
551 events were determined using built-in features in the SPASM software. Exponential fits for  
552 forward and reverse ensemble averages were performed in Origin 2019 graphing &  
553 analysis software (OriginLab).

554 Events detected in isometric optical clamping experiments were detected as  
555 described in (Takagi et al., 2006) using a zero crossing analysis via custom MATLAB scripts.  
556 Briefly, when a myosin is actively engaged with the dumbbell, force is applied to the  
557 transducer bead, a feedback loop is engaged and opposing force applied to the motor bead  
558 until the position of the transducer bead is restored. Beginnings of events are defined at the  
559 point at which the feedback signal increases from baseline in the motor bead, and ends of  
560 events are defined when the feedback signal decreases back below the baseline in the  
561 motor bead.

562

### 563 **Online supplemental material**

564 Figure S1 shows the results of a kinase assay demonstrating that Pak1, used to in  
565 purifications of phosphorylated Myo5, specifically phosphorylates Myo5 serine-357.

566 **Acknowledgements**

567

568 We thank M. Greenberg, E. Lewellyn, and A. Kunibe, each of whom played important roles

569 at the inception of this study. We thank Y.E. Goldman for optical trap instrumentation. We

570 thank M. Ferrin for helpful comments on the manuscript. This work was funded by National

571 Institute of General Medical Sciences (NIGMS) grant R35 GM118149 to D.G.D and grant

572 5R37GM057247 to E.M.O. R.T.A.P. is currently funded by NIGMS F32 GM142145.

573 **References**

574

575 Aghamohammadzadeh, S., and K.R. Ayscough. 2009. Differential requirements for actin  
576 during yeast and mammalian endocytosis. *Nat. Cell Biol.* 11:1039–1042.

577 doi:10.1038/ncb1918.

578 Akamatsu, M., R. Vasan, D. Serwas, M. Ferrin, P. Rangamani, and D.G. Drubin. 2020.

579 Principles of self-organization and load adaptation by the actin cytoskeleton during  
580 clathrin-mediated endocytosis. *Elife.* 9:1–40. doi:10.7554/eLife.49840.

581 Almeida, C.G., A. Yamada, D. Tenza, D. Louvard, G. Raposo, and E. Coudrier. 2011. Myosin 1b

582 promotes the formation of post-Golgi carriers by regulating actin assembly and  
583 membrane remodelling at the trans-Golgi network. *Nat. Cell Biol.* 13:779–789.

584 doi:10.1038/ncb2262.

585 Basu, R., E.L. Munteanu, and F. Chang. 2013. Role of turgor pressure in endocytosis in

586 fission yeast. *Mol. Biol. Cell.* 25:679–87. doi:10.1091/mbc.E13-10-0618.

587 Bement, W.M., and M.S. Mooseker. 1995. TEDS rule: A molecular rationale for differential

588 regulation of myosins by phosphorylation of the heavy chain head. *Cell Motil.*

589 *Cytoskeleton.* 31:87–92. doi:10.1002/cm.970310202.

590 Bieling, P., T. Li, J. Weichsel, R. MCGorty, P. Jreij, B. Huang, D.A. Fletcher, and R.D. Mullins.

591 2016. Force Feedback Controls Motor Activity and Mechanical Properties of Self-

592 Assembling Branched Actin Networks. *Cell.* 164:115–127.

593 doi:10.1016/j.cell.2015.11.057.

594 Blackwell, T., W.T. Stump, S.R. Clippinger, and M.J. Greenberg. 2021. Computational Tool for

595 Ensemble Averaging of Single-Molecule Data. *Biophys. J.* 120:10–20.

- 596        doi:10.1016/j.bpj.2020.10.047.
- 597    Boulant, S., C. Kural, J.-C. Zeeh, F. Ubelmann, and T. Kirchhausen. 2011. Actin dynamics  
598        counteract membrane tension during clathrin-mediated endocytosis. *Nat. Cell Biol.*  
599        13:1124–31. doi:10.1038/ncb2307.
- 600    Brzeska, H., U.G. Knaus, Z.Y. Wang, G.M. Bokoch, and E.D. Korn. 1997. p21-activated kinase  
601        has substrate specificity similar to Acanthamoeba myosin I heavy chain kinase and  
602        activates Acanthamoeba myosin I. *Proc. Natl. Acad. Sci. U. S. A.* 94:1092–1095.
- 603    Busch, D.J., J.R. Houser, C.C. Hayden, M.B. Sherman, E.M. Lafer, and J.C. Stachowiak. 2015.  
604        Intrinsically disordered proteins drive membrane curvature. *Nat. Commun.* 6.  
605        doi:10.1038/ncomms8875.
- 606    Cail, R.C., C.R. Shirazinejad, and D.G. Drubin. 2022. Induced nanoscale membrane curvature  
607        bypasses the essential endocytic function of clathrin. *J. Cell Biol.* 221.  
608        doi:10.1083/jcb.202109013.
- 609    Carlsson, A.E. 2018. Membrane bending by actin polymerization. *Curr. Opin. Cell Biol.* 50:1–  
610        7. doi:10.1016/j.ceb.2017.11.007.
- 611    Chen, C., M.J. Greenberg, J.M. Laakso, E.M. Ostap, Y.E. Goldman, and H. Shuman. 2012.  
612        Kinetic schemes for post-synchronized single molecule dynamics. *Biophys. J.* 102.  
613        doi:10.1016/j.bpj.2012.01.054.
- 614    Cheng, J., A. Grassart, and D.G. Drubin. 2012. Myosin 1E coordinates actin assembly and  
615        cargo trafficking during clathrin-mediated endocytosis. *Mol. Biol. Cell.* 23:2891–904.  
616        doi:10.1091/mbc.E11-04-0383.
- 617    Dannhauser, P.N., and E.J. Ungewickell. 2012. Reconstitution of clathrin-coated bud and  
618        vesicle formation with minimal components. *Nat. Cell Biol.* 14:634–639.

- 619       doi:10.1038/ncb2478.
- 620   Evangelista, M., B.M. Klebl, A.H. Yong, B.A. Webb, T. Leeuw, E. Leberer, M. Whiteway, D.Y.
- 621       Thomas, and C. Boone. 2000. A Role for Myosin-I in Actin Assembly through
- 622       Interactions with Vrp1p, Bee1p, and the Arp2/3 Complex. *J. Cell Biol.* 148:353–362.
- 623       doi:10.1083/jcb.148.2.353.
- 624   Geli, M.I., and H. Riezman. 1996. Role of Type I Myosins in Receptor-Mediated Endocytosis
- 625       in Yeast. *Science.* 272:533–535.
- 626   Geli, M.I., A. Wesp, and H. Riezman. 1998. Distinct functions of calmodulin are required for
- 627       the uptake step of receptor-mediated endocytosis in yeast: The type I myosin Myo5p is
- 628       one of the calmodulin targets. *EMBO J.* 17:635–647. doi:10.1093/emboj/17.3.635.
- 629   Goodson, H. V, B.L. Anderson, H.M. Warrick, L.A. Pon, and J.A. Spudich. 1996. Synthetic
- 630       lethality screen identifies a novel yeast myosin I gene (MYO5): myosin I proteins are
- 631       required for polarization of the actin cytoskeleton. *J. Cell Biol.* 133:1277–1291.
- 632       doi:10.1083/JCB.133.6.1277.
- 633   Greenberg, M.J., T. Lin, Y.E. Goldman, H. Shuman, and E.M. Ostap. 2012. Myosin IC generates
- 634       power over a range of loads via a new tension-sensing mechanism. *Proc. Natl. Acad.*
- 635       *Sci. U. S. A.* 109:E2433-40. doi:10.1073/pnas.1207811109.
- 636   Greenberg, M.J., and E.M. Ostap. 2013. Regulation and control of myosin-I by the motor and
- 637       light chain-binding domains. *Trends Cell Biol.* 23:81–9. doi:10.1016/j.tcb.2012.10.008.
- 638   Greenberg, M.J., H. Shuman, and E.M. Ostap. 2017. Measuring the Kinetic and Mechanical
- 639       Properties of Non-processive Myosins Using Optical Tweezers. *Methods Mol. Biol.*
- 640       1486:483–509. doi:10.1201/b22505.
- 641   Grosshans, B.L., H. Grötsch, D. Mukhopadhyay, I.M. Fernández, J. Pfannstiel, F.-Z. Idrissi, J.



- 642 Lechner, H. Riezman, and M.I. Geli. 2006. TEDS site phosphorylation of the yeast  
643 myosins I is required for ligand-induced but not for constitutive endocytosis of the G  
644 protein-coupled receptor Ste2p. *J. Biol. Chem.* 281:11104–14.  
645 doi:10.1074/jbc.M508933200.
- 646 Hassinger, J.E., G. Oster, D.G. Drubin, and P. Rangamani. 2017. Design principles for robust  
647 vesiculation in clathrin-mediated endocytosis. *Proc. Natl. Acad. Sci. U. S. A.* 114:E1118–  
648 E1127. doi:10.1073/pnas.1617705114.
- 649 Idrissi, F.-Z., A. Blasco, A. Espinal, and M.I. Geli. 2012. Ultrastructural dynamics of proteins  
650 involved in endocytic budding. *Proc. Natl. Acad. Sci. U. S. A.* 109:E2587–E2594.  
651 doi:10.1073/pnas.1202789109.
- 652 Idrissi, F.Z., H. Grötsch, I.M. Fernández-Golbano, C. Presciatto-Baschong, H. Riezman, and  
653 M.I. Geli. 2008. Distinct acto/myosin-I structures associate with endocytic profiles at  
654 the plasma membrane. *J. Cell Biol.* 180:1219–1232. doi:10.1083/jcb.200708060.
- 655 Joensuu, M., I. Belevich, O. Rämö, I. Nevzorov, H. Vihinen, M. Puhka, T.M. Witkos, M. Lowe,  
656 M.K. Vartiainen, and E. Jokitalo. 2014. ER sheet persistence is coupled to myosin 1c-  
657 regulated dynamic actin filament arrays. *Mol. Biol. Cell.* 25:1111–1126.  
658 doi:10.1091/mbc.E13-12-0712.
- 659 Jonsdottir, G. a., and R. Li. 2004. Dynamics of Yeast Myosin I: Evidence for a Possible Role in  
660 Scission of Endocytic Vesicles. *Development.* 14:1604–1609. doi:10.1016/j.
- 661 Jontes, J.D., E.M. Wilson-Kubalek, and R.A. Milligan. 1995. A 32 degree tail swing in brush  
662 border myosin I on ADP release. *Nature.* 378:751–753. doi:10.1038/378751a0.
- 663 Kaksonen, M., Y. Sun, and D.G. Drubin. 2003. A pathway for association of receptors,  
664 adaptors, and actin during endocytic internalization. *Cell.* 115:475–87.

- 665 Kaksonen, M., C.P. Toret, and D.G. Drubin. 2005. A modular design for the clathrin- and  
666 actin-mediated endocytosis machinery. *Cell*. 123:305–20.  
667 doi:10.1016/j.cell.2005.09.024.
- 668 Kaplan, C., S.J. Kenny, X. Chen, J. Schöneberg, E. Sitarska, A. Diz-Muñoz, M. Akamatsu, K. Xu,  
669 and D.G. Drubin. 2022. Load adaptation by endocytic actin networks. *Mol. Biol. Cell*. 33.  
670 doi:10.1091/mbc.E21-11-0589.
- 671 Krendel, M., E.K. Osterweil, and M.S. Mooseker. 2007. Myosin 1E interacts with  
672 synaptojanin-1 and dynamin and is involved in endocytosis. *FEBS Lett*. 581:644–50.  
673 doi:10.1016/j.febslet.2007.01.021.
- 674 De La Cruz, E.M., and E.M. Ostap. 2009. Kinetic and Equilibrium Analysis of the Myosin  
675 ATPase. *Methods Enzymol*. 455:157–192. doi:10.1016/S0076-6879(08)04206-7.
- 676 Laakso, J.M., J.H. Lewis, H. Shuman, and E.M. Ostap. 2008. Myosin I can act as a molecular  
677 force sensor. *Science*. 321:133–6. doi:10.1126/science.1159419.
- 678 Laakso, J.M., J.H. Lewis, H. Shuman, and E.M. Ostap. 2010. Control of myosin-I force sensing  
679 by alternative splicing. *Proc. Natl. Acad. Sci. U. S. A.* 107:698–702.  
680 doi:10.1073/pnas.0911426107.
- 681 Lewellyn, E.B., R.T. Pedersen, J. Hong, R. Lu, H.M. Morrison, and D.G. Drubin. 2015. An  
682 Engineered Minimal WASP-Myosin Fusion Protein Reveals Essential Functions for  
683 Endocytosis. *Dev. Cell*. 35:281–294. doi:10.1016/j.devcel.2015.10.007.
- 684 Lewis, J.H., T. Lin, D.E. Hokanson, and E.M. Ostap. 2006. Temperature dependence of  
685 nucleotide association and kinetic characterization of Myo1b. *Biochemistry*. 45:11589–  
686 97. doi:10.1021/bi0611917.
- 687 Lin, T., N. Tang, and E.M. Ostap. 2005. Biochemical and motile properties of Myo1b splice

688 isoforms. *J. Biol. Chem.* 280:41562–41567. doi:10.1074/jbc.M508653200.

689 Manenschijn, H.E., A. Picco, M. Mund, J. Ries, and M. Kaksonen. 2019. Type-I myosins  
690 promote actin polymerization to drive membrane bending in endocytosis. *Elife.*  
691 17:490011. doi:10.1101/490011.

692 El Mezgueldi, M., N. Tang, S.S. Rosenfeld, and E.M. Ostap. 2002. The Kinetic Mechanism of  
693 Myo1e (Human Myosin-IC ). *J. Biol. Chem.* 277. doi:10.1074/jbc.M200713200.

694 Mogilner, A., and G. Oster. 1996. Cell motility driven by actin polymerization. *Biophys. J.*  
695 71:3030–3045. doi:10.1016/S0006-3495(96)79496-1.

696 Mogilner, A., and G. Oster. 2003. Force Generation by Actin Polymerization II: The Elastic  
697 Ratchet and Tethered Filaments. *Biophys. J.* 84:1591–1605. doi:10.1016/S0006-  
698 3495(03)74969-8.

699 Mund, M., J.A. Van Der Beek, J. Deschamps, S. Dmitrieff, P. Hoess, J.L. Monster, A. Picco, F.  
700 Nedelec, M. Kaksonen, and J. Ries. 2018. Systematic Nanoscale Analysis of Endocytosis  
701 Links Efficient Vesicle Formation to Patterned Actin Nucleation. *Cell.* 174:884–896.  
702 doi:10.1016/j.cell.2018.06.032.

703 Nickaen, M., J. Berro, T.D. Pollard, and B.M. Slepchenko. 2019. Actin assembly produces  
704 sufficient forces for endocytosis in yeast. *Mol. Biol. Cell.* 30:2014–2024.  
705 doi:10.1091/mbc.E19-01-0059.

706 Pedersen, R.T., and D.G. Drubin. 2019. Type I myosins anchor actin assembly to the plasma  
707 membrane during clathrin-mediated endocytosis. *J. Cell Biol.* 218:1138–1147.  
708 doi:10.1083/jcb.201810005.

709 Picco, A., M. Mund, J. Ries, F. Nedelec, and M. Kaksonen. 2015. Visualizing the functional  
710 architecture of the endocytic machinery. *Elife.* 4:1–29. doi:10.7554/eLife.04535.

- 711 Pyrpassopoulos, S., G. Arpağ, E.A. Feeser, H. Shuman, E. Tüzel, and E.M. Ostap. 2016. Force  
712 generation by membrane-associated myosin-I. *Sci. Rep.* 6:1–14.  
713 doi:10.1038/srep25524.
- 714 Roy, M.A., N. Siddiqui, and D. D’Amours. 2011. Dynamic and selective DNA-binding activity  
715 of Smc5, a core component of the Smc5-Smc6 complex. *Cell Cycle.* 10:690–700.  
716 doi:10.4161/cc.10.4.14860.
- 717 Skruzny, M., T. Brach, R. Ciuffa, S. Rybina, M. Wachsmuth, and M. Kaksonen. 2012.  
718 Molecular basis for coupling the plasma membrane to the actin cytoskeleton during  
719 clathrin-mediated endocytosis. *Proc. Natl. Acad. Sci. U. S. A.* 109:E2533–E2542.  
720 doi:10.1073/pnas.1207011109.
- 721 Snoberger, A., B. Barua, J.L. Atherton, H. Shuman, E. Forgacs, Y.E. Goldman, D.A.  
722 Winkelmann, and E.M. Ostap. 2021. Myosin with hypertrophic cardiac mutation r712l  
723 has a decreased working stroke which is rescued by omecamtiv mecarbil. *Elife.* 10:1–  
724 24. doi:10.7554/eLife.63691.
- 725 Sokac, A.M., C. Schietroma, C.B. Gundersen, and W.M. Bement. 2006. Myosin-1c couples  
726 assembling actin to membranes to drive compensatory endocytosis. *Dev. Cell.* 11:629–  
727 40. doi:10.1016/j.devcel.2006.09.002.
- 728 Spudich, J.A., and S. Watt. 1971. The Regulation of Rabbit Skeletal Muscle Contraction. *J.*  
729 *Biol. Chem.* 246:4866–4871.
- 730 Stewart, T.J., V. Murthy, S.P. Dugan, and J.E. Baker. 2021. Velocity of myosin-based actin  
731 sliding depends on attachment and detachment kinetics and reaches a maximum when  
732 myosin-binding sites on actin saturate. *J. Biol. Chem.* 297.  
733 doi:10.1016/j.jbc.2021.101178.

- 734 Sun, Y., A.C. Martin, and D.G. Drubin. 2006. Endocytic Internalization in Budding Yeast  
735 Requires Coordinated Actin Nucleation and Myosin Motor Activity. *Dev. Cell.* 11:33–46.  
736 doi:10.1016/j.devcel.2006.05.008.
- 737 Sun, Y., J. Schöneberg, X. Chen, T. Jiang, C. Kaplan, K. Xu, T.D. Pollard, and D.G. Drubin. 2019.  
738 Direct comparison of clathrin-mediated endocytosis in budding and fission yeast  
739 reveals conserved and evolvable features. *Elife.* 8. doi:10.7554/eLife.50749.
- 740 Takagi, Y., E.E. Homsher, Y.E. Goldman, and H. Shuman. 2006. Force generation in single  
741 conventional actomyosin complexes under high dynamic load. *Biophys. J.* 90:1295–  
742 1307. doi:10.1529/biophysj.105.068429.
- 743 Veigel, C., L.M. Coluccio, J.D. Jontes, J.C. Sparrow, R. a Milligan, and J.E. Molloy. 1999. The  
744 motor protein myosin-I produces its working stroke in two steps. *Nature.* 398:530–  
745 533. doi:10.1038/19104.
- 746 Woody, M.S., M.J. Greenberg, B. Barua, D.A. Winkelmann, Y.E. Goldman, and E.M. Ostap.  
747 2018. Positive cardiac inotrope omecamtiv mecarbil activates muscle despite  
748 suppressing the myosin working stroke. *Nat. Commun.* 9. doi:10.1038/s41467-018-  
749 06193-2.
- 750 Woody, M.S., J.H. Lewis, M.J. Greenberg, Y.E. Goldman, and E.M. Ostap. 2016. MEMLET: An  
751 Easy-to-Use Tool for Data Fitting and Model Comparison Using Maximum-Likelihood  
752 Estimation. *Biophys. J.* 111:273–282. doi:10.1016/j.bpj.2016.06.019.
- 753 Woody, M.S., E.M. Ostap, Y.E. Goldman, and M. Capitanio. 2017. An ultra-fast EOD-based  
754 force-clamp detects rapid biomechanical transitions. *SPIE-Intl Soc Optical Eng.* 26.  
755

756 **Figure 1: Models for the functions of actin assembly and myosin activity during**  
757 **membrane deformation for clathrin-mediated endocytosis**

758 Cartoon diagram illustrating the organization of actin filaments and Myo5 molecules at  
759 endocytic sites. Actin filaments are bound by coat proteins at the tip of the growing  
760 membrane invagination and oriented with their growing ends toward the plasma  
761 membrane, powering membrane invagination. The type I myosin Myo5 could either anchor  
762 the actin network in a favorable orientation (left) or provide an assisting force (right).

763

764 **Figure 2: In-solution, population biochemical characterization of Myo5**

765 **(A)** Coomassie-stained SDS-polyacrylamide gels showing example preparations of the  
766 purified Myo5 motor/lever construct and calmodulin (Cmd1, light chain) used in all  
767 experiments. **(B)** The actin concentration dependence of the steady-state ATPase activity of  
768 100 nM unphosphorylated (grey circles) and phosphorylated Myo5 (black circles). Each  
769 data point represents the average of 6-7 time courses, which were 100 s each. The orange  
770 line is a best fit of the phosphorylated Myo5 data to a rectangular hyperbola. **(C)** Schematic  
771 pathway for the Myo5 ATPase cycle. Blue motors are in tightly bound conformations, green  
772 motors are weakly bound/unbound. **(D)** Example light scattering transients reporting on  
773 ATP-induced dissociation of phosphorylated (left,  $k_{\text{obs}} = 17 \text{ s}^{-1}$ ) and unphosphorylated  
774 (right,  $k_{\text{obs}} = 64.1 \text{ s}^{-1}$ ) actoMyo5, obtained by mixing 100 nM actoMyo5 (AM) with 94  $\mu\text{M}$   
775 and 72  $\mu\text{M}$  ATP, respectively, as shown in the inset schematic. The black line is the fit of a  
776 single exponential function to the data. **(E)** ATP concentration dependence of dissociation  
777 of 100 nM unphosphorylated (grey circles) and phosphorylated actoMyo5 (black circles).  
778 Each data point represents 3-6 time courses averaged and fit to a single exponential decay

779 function. The orange line is a linear best fit of the phosphorylated Myo5 data. The purple  
780 line is a best fit of the unphosphorylated Myo5 data to a rectangular hyperbola.  
781 **(F)** Example light scattering transients reporting ATP-induced dissociation of ADP-  
782 saturated phosphorylated (left) and unphosphorylated (right) actoMyo5, obtained by  
783 preincubating 200 nM actoMyo5 (AM) with 100  $\mu$ M ADP, then mixing rapidly with 2.5 mM  
784 ATP, as shown in the inset schematic. The black line is the fit of a single exponential  
785 function to the data. **(G)** Velocity of actin filament gliding, measured at varying surface  
786 densities of Phospho-Myo5 (black circles, orange line) and unphosphorylated Myo5 (gray  
787 circles, purple line) in in vitro motility assays. Myosin concentrations indicate the quantity  
788 of protein incubated in the flow chamber before washing. Each data point represents the  
789 average velocity of 30 – 60 filaments, and the error bars are standard deviations.

790

#### 791 **Table 1**

792 Summary of rate and equilibrium constants measured for Myo5 in this study. Errors are  
793 standard errors of the fits.

794

#### 795 **Figure 3: Single molecule, optical trap analysis of Myo5 step size and kinetics**

796 **(A)** Cartoon schematic of the 3-bead optical trapping setup. A biotinylated actin filament is  
797 tethered between two neutravidin-coated beads that are trapped in a dual beam optical  
798 trap. This bead-actin-bead “dumbbell” is lowered onto pedestal beads that have been  
799 sparsely coated with His<sub>6</sub> antibody to attach Myo5-motor/lever-Avi-Tev-His<sub>9</sub>. **(B-D)** Single  
800 Myo5 displacements of a single bead position and covariance traces, calculated using both  
801 beads, showing single molecule interactions acquired in the presence of 1  $\mu$ M **(B)** 10  $\mu$ M

802 **(C)** and 1000  $\mu\text{M}$  ATP. **(D)**. Blue bars indicate attachment events as identified by covariance  
803 (gray) decreases. The threshold of event detection by the covariance traces are indicated  
804 by dashed gray lines. **(E)** Schematic of displacement traces depicting the 2-step nature of  
805 actomyosin displacements in the optical trap. **(F-H)** Binding events were synchronized at  
806 their beginnings (left) or ends (right) and averaged forward or backward in time,  
807 respectively. Measured total displacement of Myo5 was 5.0 nm at 10  $\mu\text{M}$  ATP, with the 1<sup>st</sup>  
808 substep contributing a 4.8 nm displacement (arrow 1. in G) and the 2<sup>nd</sup> substep  
809 contributing a 0.2 nm displacement (arrow 2. In G). **(F-H, left)** Forward-averaged  
810 ensembles synchronized at the beginnings of events. **(F-H, right)** Reverse-averaged  
811 ensembles synchronized at the ends of events. Black and gray lines are single exponential  
812 fits in the forward and reverse ensembles, respectively. **(I)** Cumulative distributions of  
813 attachment durations for Myo5 at 1, 10, and 1000  $\mu\text{M}$  ATP. Blue lines show cumulative  
814 frequency of attachment durations at the indicated ATP concentrations, and the red,  
815 yellow, and green lines indicate fitted exponential distributions at 1, 10, and 1000  $\mu\text{M}$  ATP,  
816 respectively. 1 and 10  $\mu\text{M}$  ATP were fit well to single exponentials, and the 1000  $\mu\text{M}$  ATP  
817 data were best described by the sum of two exponentials. **(J)** Summary of rates at 1, 10, and  
818 1000  $\mu\text{M}$  ATP calculated from (F-H). Blue boxes are the fitted exponential distributions  
819 from (I), black diamonds are forward ensemble fits from (F-H, left), and gray diamonds are  
820 reverse ensemble fits from (F-H, right). At lower concentrations of ATP (1 and 10  $\mu\text{M}$ ), the  
821 rate of detachment is limited by ATP association, corresponding to the reverse ensemble  
822 fits, while at saturating ATP concentration (1000  $\mu\text{M}$ ), the detachment rate is limited by the  
823 rate of ADP dissociation, corresponding to the forward ensemble fits. **(K)** Summary of rates  
824 determined via single molecule optical trapping. Errors for detachment rates are 95%



825 confidence intervals. Errors for forward and reverse ensemble fits are standard errors of  
826 the fits. \*Detachment rates at 1000  $\mu\text{M}$  ATP were best fit to the sum of 2 exponents. The  
827 major component of the fit ( $67.8 \text{ s}^{-1}$ ) comprises 92.1% of the total with the remaining 7.9%  
828 having a rate of  $11.6 \text{ s}^{-1}$ .

829

830 **Figure 4: Myo5 attachment lifetimes are substantially less force-dependent than**  
831 **other known type I myosins**

832 An isometric optical force clamp was utilized to determine the force-sensitivity of the  
833 detachment of Myo5 from actin. **(A)** Durations of individual actomyosin attachments as a  
834 function of force, plotted on a semi-log scale **(B)** The solid black line shows the force  
835 dependence of the detachment rates determined by MLE fitting of unaveraged points in A.  
836 For illustration purposes, attachment durations from (A) were binned by force at every 10  
837 points, averaged, and converted to rates. Best-fit parameters were determined by MLE  
838 fitting and 95% confidence intervals were calculated via bootstrapping. The solid black line  
839 is calculated from best fit parameters ( $k = 67.6 \text{ s}^{-1}$ ,  $d = 1.14 \text{ nm}$ ), while the gray shaded  
840 region is the 95% confidence interval ( $k = 62.4\text{-}72.9 \text{ s}^{-1}$ ,  $d = 1.03\text{-}1.26 \text{ nm}$ ). All MLE fitting  
841 was performed on unaveraged data and was corrected for instrument deadtime. **(C)** The  
842 force dependent detachment rate of Myo5 (from panel B) plotted alongside the force  
843 dependent detachment rates for Myo1b, Myo1c, and  $\beta$ -cardiac muscle myosin, Myh7. **(D)**  
844 Power output for the same four myosins calculated over a range of forces by multiplying  
845 the functions from (C) by the applied force  $F$ , and the step size and duty ratios of each  
846 myosin.

847

848 **Figure S1: P21 Activated Kinase 1 (Pak1) phosphorylates Myo5 on S357**

849 Crude preparations of wild type and S357A Myo5 motor/lever constructs were mixed with  
850 250  $\mu$ M ATP including 20  $\mu$ Ci of ATP $\gamma$ P32 in kinase assay buffer (5 mM MOPS pH 7, 2.5 mM  
851  $\beta$ -glycerophosphate, 5 mM MgCl<sub>2</sub>, 400  $\mu$ M EDTA, 1 mM EGTA, 50  $\mu$ M DTT) in either the  
852 presence or absence of Pak1. Reactions were incubated at 25°C for 60 minutes, then  
853 quenched by adding an equal volume of 2x tris urea sample buffer (125 mM Tris pH 6.8,  
854 6 M urea, 2% SDS, 0.1% bromophenol blue, 10%  $\beta$ -mercaptoethanol) and resolved on a  
855 10% polyacrylamide gel. The gel was stained with Coomassie, then dried onto Whatman  
856 paper and exposed to a storage phosphor screen (Amersham). The Coomassie-stained gel  
857 was imaged on a standard photo scanner and the phosphor screen on a Typhoon gel imager  
858 (Amersham). Note that there are differences in baseline labeling in the absence of added  
859 kinase between the two different protein preps, but addition of Pak1 clearly results in  
860 radiolabeling of wild type but not mutant Myo5.

861

862 **Movie S1: Motility assays with phosphorylated Myo5**

863 Rhodamine phalloidin-labeled actin filaments gliding over coverslips coated with a  
864 concentration series of phosphorylated Myo5 protein in motility buffer with 1 mM ATP.  
865 Movies were collected at 1 frame per second and are played back at 16 frames per second.

866

867

868 **Movie S2: Motility assays with unphosphorylated Myo5**

869 Rhodamine phalloidin-labeled actin filaments gliding over coverslips coated with a  
870 concentration series of unphosphorylated Myo5 protein in motility buffer with 1 mM ATP.

871 Short movies of motility at 100 nM and 150 nM unphosphorylated Myo5 were collected  
872 because no motility was observed. Movies at all other concentrations were collected at 1  
873 frame every 4 seconds and are played back at 16 frames per second. The playback rate of  
874 Movie S2 is four times faster than the playback rate of Movie S1.

## Figure 1

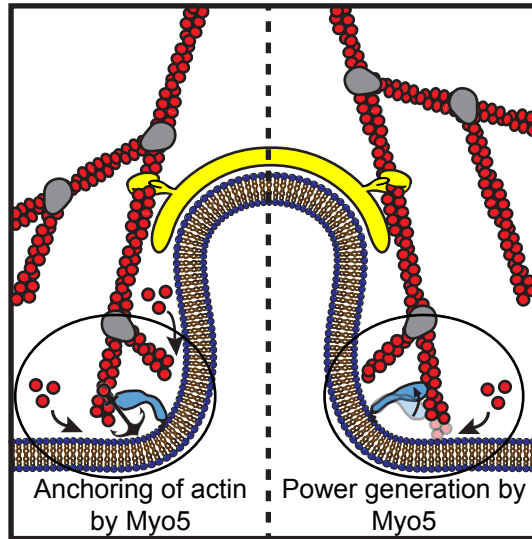
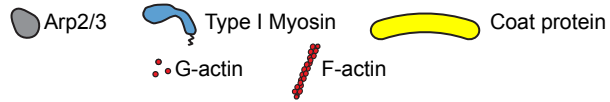


**Table 1: Rate and equilibrium constants of the Myo5 ATPase cycle**

	Phosphorylated Myo5	Unphosphorylated Myo5
<b>Steady-state</b>		
<b>actin-activated ATPase</b>		
$V_{\max}$ (s <sup>-1</sup> )	3.3 (± 0.15)	ND
$K_{\text{ATPase}}$ (μM)	5.1 (± 0.88)	ND
<b>ATP binding</b>		
$K_1'$ (μM <sup>-1</sup> )	ND	0.006 (± 0.0016)
$k_{+2}'$ (s <sup>-1</sup> )	≥ 335	290 (± 24)
$K_1'k_{+2}'$ (μM <sup>-1</sup> s <sup>-1</sup> ) <sup>a</sup>	0.39 (± 0.017) <sup>b</sup>	1.1 (± 0.28) <sup>c</sup>
<b>ADP release</b>		
$k_{+5}'$ (s <sup>-1</sup> )	74 (± 2.0)	107 (± 5.9)

<sup>a</sup>Determined from a linear fit of the unbinding rates. <sup>b</sup>Linear fit of all data for Phosphorylated Myo5 in Fig. 2E. <sup>c</sup>Linear fit of observed rates below 100 μM ATP for Unphosphorylated Myo5 in Fig 2E. ND: Not Determined.

## Figure 2

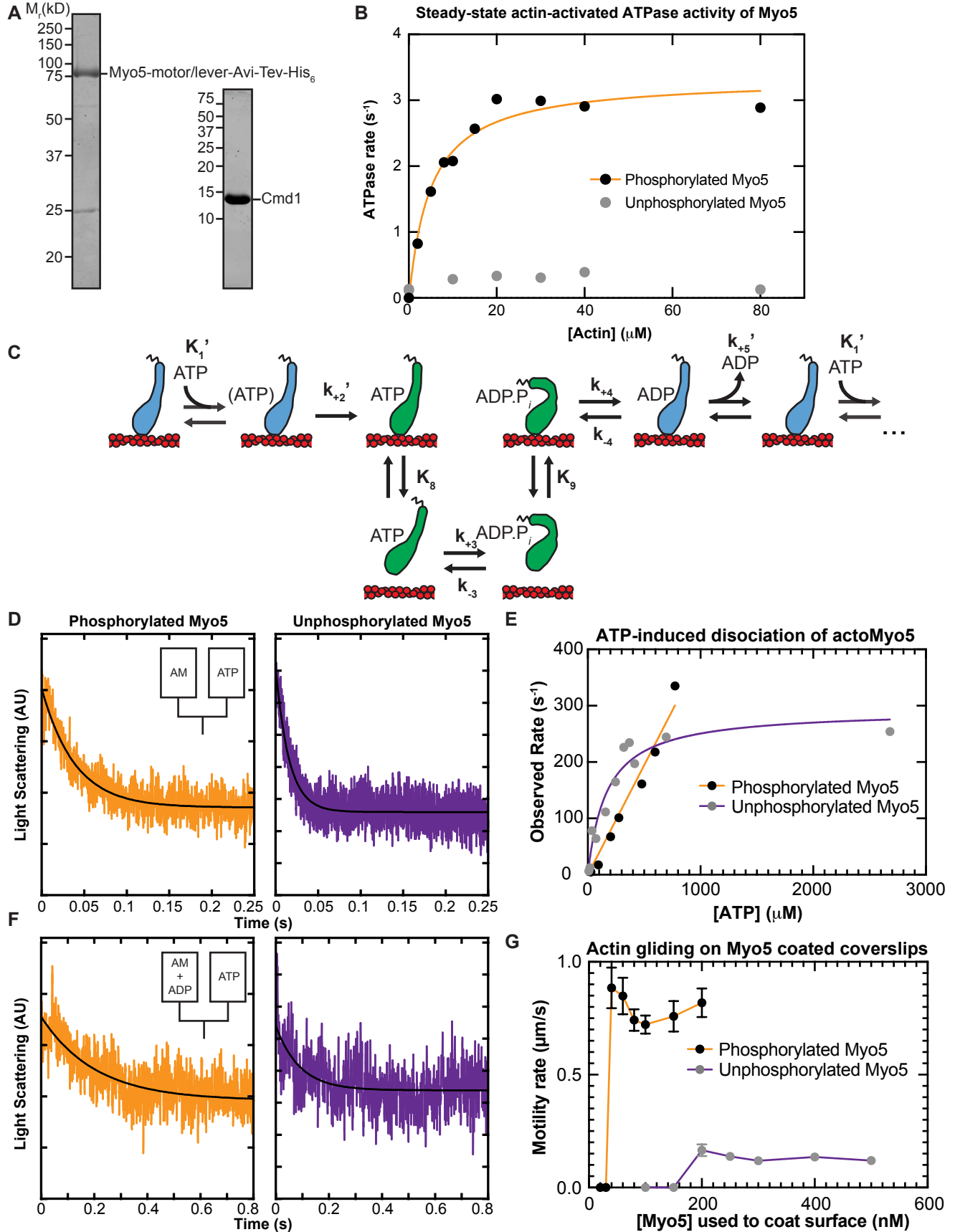
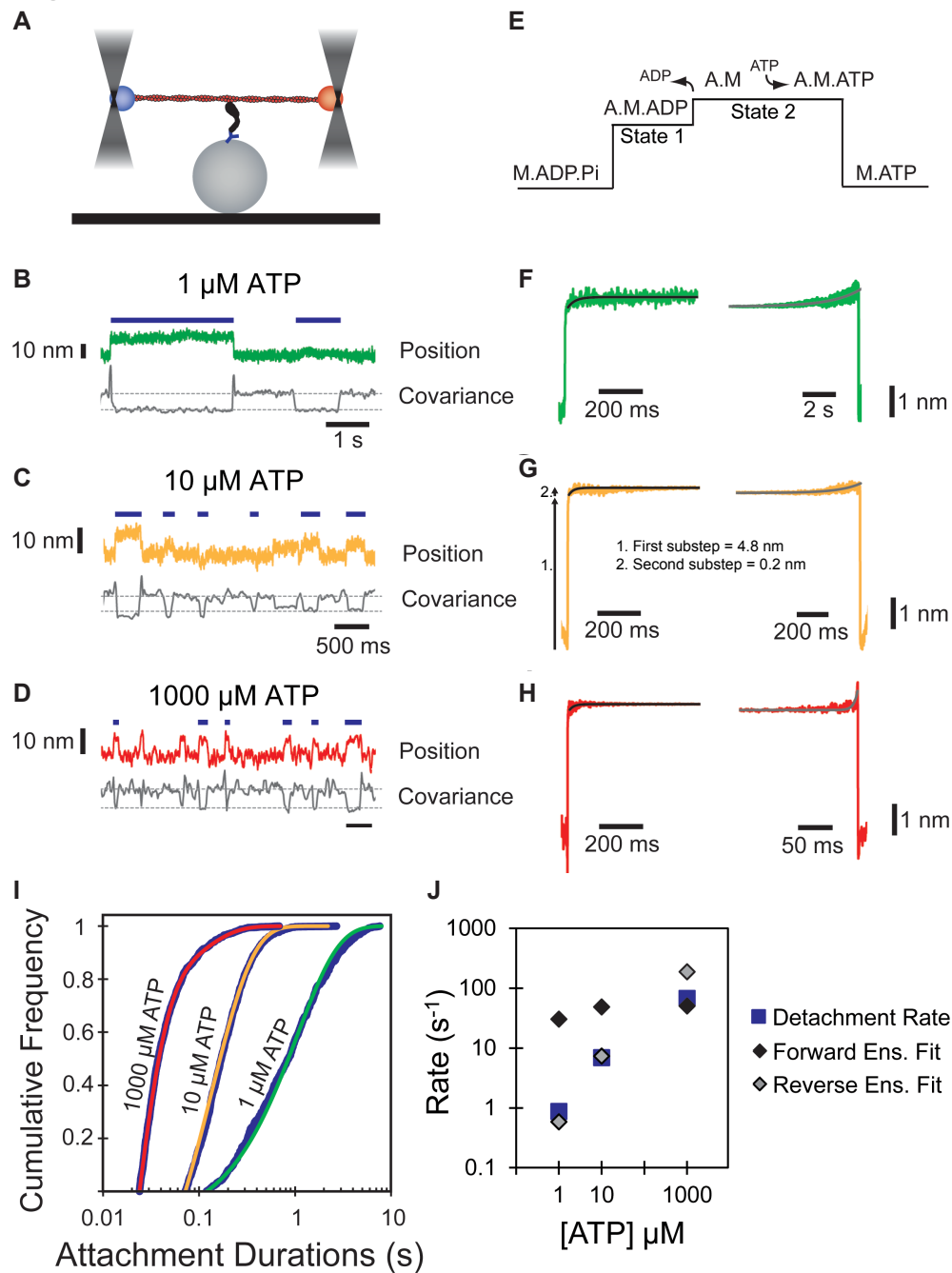


## Figure 3



### K Summary of rates determined during single molecule optical trapping

[ATP] $\mu\text{M}$	Detachment Rate ( $\text{s}^{-1}$ )	Forward Ensemble Fit ( $\text{s}^{-1}$ )	Reverse Ensemble Fit ( $\text{s}^{-1}$ )
1	0.88 (+/- 0.07/0.07)	>30	0.59 (+/- 0.003)
10	6.9 (+/- 0.49/0.46)	49 (+/- 1.6)	7.3 (+/- 0.1)
1000	67.8* (+/- 11.9/8.7)	50 (+/- 0.2)	>187

**Figure 4**

